Assimilation of Meteosat Third Generation (MTG) Lightning Imager (LI) obervations in AROME-France – Proof of Concept

Felix Erdmann[1,2], Olivier Caumont[1,3,*], and Eric Defer[4,*]

[1]CNRM, Université de Toulouse, Météo-France, CNRS, Toulouse, France
[2]Royal Meteorological Institute, 3 av Circulaire, 1180 Brussels, Belgium
[3]Météo-France, Direction des opérations pour la prévision, Toulouse, France
[4]Laboratoire d'Aérologie, 14 avenue Edouard Belin, 31400 Toulouse, France
[*]These authors contributed equally to this work.

Correspondence: Felix Erdmann (felix.erdmann@meteo.be)

Abstract. This study develops a Lightning Data Assimilation (LDA) scheme for the regional, convection-permitting NWP model AROME-France. The LDA scheme intends to assimilate total lightning, i.e., cloud-to-ground (CG) and inter- and intra-cloud (IC), of the future Meteosat Third Generation (MTG) Lightning Imager (LI). MTG-LI proxy data are created and Flash Extent Density (FED) fields are derived. An FED forward observation operator (FFO) is trained based on modeled, column integrated graupel mass from 24 storm days in 2018. The FFO is successfully verified for 2 independent storm days. With the FFO, the LDA adapts a 1-dimensional Bayesian (1DBay) retrieval followed by a 3-dimensional variational (3DVar) assimilation approach that is currently run operationally in AROME-France for radar reflectivity data. The 1DBay retrieval derives relative humidity profiles from the background by comparing the FED observations to the FED inferred from the background. Retrieved relative humidity profiles are assimilated as sounding data. The evaluation of the LDA comprises different LDA experiments and four case studies. It is found that all LDA experiments can increase the background integrated water vapor (IWV) in regions where the observed FED exceeds the FED inferred from AROME-France outputs. In addition, IWV can be reduced where spurious FED is modeled. A qualitative analysis of 6-hour accumulated rainfall fields reveals that the LDA is capable of locating and initiating some local precipitation fields better than a radar data assimilation (RDA) experiment. However, the LDA also leads to too high rainfall accumulations at some locations. Fractions Skill Scores (FSSs) of 6-hour accumulated rainfall are overall similar for the developed LDA and RDA experiments. An approach aiming at mitigating effects due to differences in the optical extents of lightning flashes and the area of the corresponding cloud was developed and included in the LDA, however, it does not always improve the FSS.

1 Introduction

Convective weather phenomena such as thunderstorms threaten the society by producing severe weather and related impacts, e.g., flash floods, large hail, tornadoes, and strong winds. Cloud electrification and subsequent lightning discharges are caused by interactions of different ice particles inside convective clouds. The process makes lightning an effective tracer of deep convection. The new type of lightning locating systems (LLSs) on geostationary (GEO) satellites allows for continuous large-

scale monitoring of total, i.e., cloud-to-ground (CG) and inter/intra-cloud (IC), lightning activity. The Geostationary Lightning Mappers (GLMs) on the GOES-R series satellites cover the Americas and the adjacent oceans (Goodman et al., 2013). A

25 similar instrument, the Meteosat Third Generation (MTG) Lightning Imager (LI), will be launched in the 2022 time-frame to monitor lightning over among others Europe, Africa, and wide parts of the Atlantic Ocean (Dobber and Grandell, 2014). GEO lightning sensors provide continuous high-frequency observations of the total lightning activity over a wide domain. High-quality GEO data is also available in data-sparse regions with limited access, such as over oceans and mountainous terrain as well as countries without radar networks. GEO lightning data may become important for numerical weather prediction (NWP),

30 potentially improving the initial state of the model and the accuracy of the predicted storm location, timing, and intensity. The lightning data assimilation (LDA) addresses this objective.

LDA is not trivial. Operational models, e.g., the Application of Research to Operations at Mesoscale (AROME) model (Brousseau et al., 2016), the regional operational model of Météo-France, do not include any explicit representation of lightning. Other difficulties of lightning data assimilation include the ephemeral nature of lightning relative to the life cycle of

35 thunderstorm and time-space shifts between observations and the background, which are usual at the storm scale, challenge up-to-date data assimilation systems (zero-spread, zero-gradient problems) (e.g., Janisková and Lopez, 2013). Background errors are not Gaussian, and lightning is more related to lower-impact variables such as hydrometeor content and vertical velocity than to thermodynamic variables. Despite the difficulties, former studies have shown the benefits of LDA for forecasts of convection and related phenomena.

40 Early LDA studies used NWP models that parametrize convection. Lightning data controlled the activation of the convective parametrization scheme (CPS). Often nudging techniques were applied to modify the model humidity and wind fields (e.g., Papadopoulos et al., 2005; Mansell et al., 2007; Lagouvardos et al., 2013; Giannaros et al., 2016), or latent heat (e.g., Pessi and Businger, 2009). These studies reported positive effects of LDA on the score of precipitation forecasts, especially for the location and quantity of heavy rain.

45 When NWP models resolve convection (<3 km horizontal resolution), so-called lightning proxies can be used to relate NWP output to lightning observations. Some former studies suggested and tested cloud top height, cloud top pressure, and cold cloud depth as predictors to estimate the lightning density (e.g., Price and Rind, 1992, 1993; Wong et al., 2013; Giannaros et al., 2015; Karagiannidis et al., 2019).

Recent development corroborates using cloud dynamics or ice hydrometeors, e.g., graupel for reliable lightning proxies.

50 Indeed, field campaigns as those reported by Deierling et al. (2008) found a strong correlation between lightning activity and ice mass fluxes. Deierling and Petersen (2008) showed a robust relationship between total lightning rate and updraft characteristics, especially the updraft volume. Buiat et al. (2017) analyzed CloudSat Cloud Profiling Radar (CPR) to relate cloud ice water content (IWC) and effective radius (ER) to LINET (Betz et al., 2009) lightning strokes. They found that high IWC and high ER are favorable to CG strokes. Graupel contributes to both high IWC and high ER. Strong on-going updraughts

55 can cause high IWC. Hence, the findings agree with the studies of Deierling et al. (2008); Deierling and Petersen (2008).

Various lightning proxies have been tested in NWP studies. McCaul et al. (2009) brought forward two lightning proxies based on ice-phase hydrometeor fields, one related to upward fluxes and the second related to vertically integrated content,

in the WRF model. Relating domain-wide statistics of peaks in the proxy fields to peaks of the flash rate density, a blended solution using both proxies is suggested to reproduce both temporal variability and areal coverage of the lightning observations.

60 Yair et al. (2010) introduced a lightning potential index (LPI) that is calculated using the simulated grid-scale vertical velocity and simulated hydrometeor mass mixing ratios of liquid water, cloud ice, snow, and graupel. Barthe et al. (2010) concluded that none of precipitation ice mass, ice water path, ice mass flux product, updraft volume, maximum vertical velocity, and cloud top height could predict the lightning flash rates and trends well for both of their two cases. Formenton et al. (2013) confirms a key role of graupel in the cloud electrification, as described in the non-inductive charging mechanism, in their 1D model.

65 Federico et al. (2014) simulate lightning based on graupel carrying negative charge and ice carry positive charge. Bovalo et al. (2019) recommended graupel mass as most reliable proxy for lightning location and peak flash rate after analyzing eight test cases. Their cell scale approach resulted in more robust relationships than a domain scale approach.

With the lightning proxies, lightning observation operators are created to compare the model output to the lightning observations and assimilate the lightning data. Most of the recent LDA schemes use lightning operators based on ice hydrometeors or

70 updraft characteristics, e.g., graupel mass or updraft volume. In the following, a brief overview of LDA techniques is presented, with the focus on 3-dimensional variational (3DVar) LDA and studies to assimilate GLM data.

Fierro et al. (2012) put forward a widely used (e.g., Dixon et al., 2016; Wang et al., 2017a; Federico et al., 2017; Wang et al., 2017b) concept of lightning proxy calculating water vapor mixing ratio from simulated graupel mass and observed flash rates. They then increased the water vapor mixing ratio in the $0\,^{\circ}\mathrm{C}$ to $-20\,^{\circ}\mathrm{C}$ layer where lightning was observed and the

75 relative humidity (RH) of the background was less than $81\,\%$. Precipitating convection was better correlated with observed reflectivity fields for the LDA than for the control experiment. The method was further tested by Fierro et al. (2014) using 10-minute Flash Extent Density (FED). Lynn et al. (2015); Marchand and Fuelberg (2014) refined the nudging technique of Fierro et al. (2012) to increase the virtual temperature perturbation and favor static instability or by warming the source layer of the convective updraft, respectively. Lynn et al. (2015) also introduced an extension to suppress spurious convection.

80 Qie et al. (2014) constructed empirical formulas between total lightning and graupel, ice, and snow mixing ratios based on thunderstorms over northern China. Lightning data were used by Wang et al. (2014) to generate pseudo radar reflectivity which was subsequently assimilated using the physical initialization method to adjust model variables. Wang et al. (2018) used time-lagged ensemble forecasts to retrieve q_g from lightning rates.

Mansell (2014); Allen et al. (2016) assimilated synthetic GLM total lightning represented as FED using an Ensemble Kalman

85 Filter (EnKF) with positive effects on predicted spurious convection, updraft locations, and reflectivity. Mansell (2014) used both the simulated flash rate and a linear relationship between total lightning and graupel volume as observation operators. Allen et al. (2016) tested observation operators in the sense of a linear best fit operator. They found that graupel mass and graupel volume yield better results than an operator based on the non-inductive charging rate. In preparation of a hybrid variational-ensemble LDA technique for GLM, Apodaca et al. (2014) assimilated World Wide Lightning Location Network

90 (WWLLN) data in WRF. However, the use of WWLLN as a GLM proxy is debatable as WWLLN mainly detects CG flashes, whereas GLM detects total lightning.

A 3DVar LDA was applied by Wang et al. (2017b) using the relationship given by Fierro et al. (2012) to retrieve water vapor mixing ratio q_v from total flash rates. The q_v is then transformed to RH in the form of sounding data and assimilated as such. They noted increased forecasts skills in general, but also that the method still needs improvement to suppress spurious convection. Fierro et al. (2016) replaced their previous nudging by a 3DVar LDA. Pseudo-q_v profiles were created through saturation of modeled q_v-profiles between the lifted condensation level (LCL) and $15\,\mathrm{km}$ if 10-minute FED exceeded 50 flashes per pixel. They found that the Radar Data Assimilation (RDA) yielded better forecasts of convective cells during the first $30\,\mathrm{min}$ of the forecast, while the LDA gave better storm structures at about one-hour forecast. The combination of both RDA and LDA provided the highest forecast skill. Fierro et al. (2019) tested this 3DVar assimilation technique developed for ground-based data with GLM total lightning observations. The LDA method adjusts water vapor mass mixing ratio within a fixed layer depth above the LCL by assuming nearly water-saturated conditions at observed lightning locations. It adds q_v in regions of lightning regardless of flash rate by setting RH to $95\,\%$ in a layer of $3\,\mathrm{km}$ above the LCL if the background RH is less than $95\,\%$. Both LDA and RDA improved the short-term accumulated precipitation and radar reflectivity composite. However, the LDA scheme of Fierro et al. (2019) is not able to suppress spurious convection although one experiment balanced the total water vapor mass added by the LDA by an equal removal outside observed lightning locations. Hu et al. (2020) adopted the technique of Fierro in their cloud-scale model with $1.5\,\mathrm{km}$ horizontal resolution and found, as also previously reported, a wet bias in the model that increased with the forecast time. The method still misses a suppression of spurious convection in regions without lightning. They also conducted a layer depth sensitivity study with similar results for adding q_v in layers of $2\,\mathrm{km}$ to $10\,\mathrm{km}$ depth. Kong et al. (2020) present an LDA of real GLM data in an EnKF framework. FED at $10\,\mathrm{km}$ pixel resolution is assimilated using both graupel mass and graupel volume-based observation operators. Both LDAs could produce model-consistent analyses of the state variables and improved the forecast especially for regions of deep moist convection in an MCS environment. Liu et al. (2020) assimilated Chinese satellite Fengyun-4 (FY4) lightning and cloud top data. Pseudo-RH profiles were created by setting the RH to $90\,\%$ where lightning was observed and the background RH was less than $90\,\%$. Two methods using the LCL and measured cloud tops improve the equitable threat score for precipitation forecasts the most, whereas only the approach with fixed top height produced spurious convection in one case. Chen et al. (2020) assimilated FY4 lightning data by retrieving maximum proxy-reflectivity from the lightning data via a logarithmic relationship. Maximum proxy-reflectivity is then extended to 3D pseudo-reflectivity profiles and eventually assimilated.

The main goal of this work is to develop a 3DVar LDA for MTG-LI data to improve analyses and forecasts, especially in convective situations. Pseudo-observations of the MTG-LI are generated to form the lightning data base (Section 3). A novel LDA scheme is developed for the regional, operational, convective-scale model AROME-France of Météo-France. Different assimilation approaches including the presence and absence of radar reflectivity, Doppler wind velocity, and FED in the set of assimilated observations are compared to assess the added value of the developed LDA. Recent Var LDAs using GLM data, e.g., Fierro et al. (2019); Hu et al. (2020) cannot suppress spurious convection. Our LDA of GEO lightning data should promote convection if needed and also suppress spurious convection.

The NWP model configuration and lightning data as used for this work are briefly explained in Sections 2 and 3, respectively. Section 4 reviews lightning observation operators and introduces the lightning observation operator developed for this study.
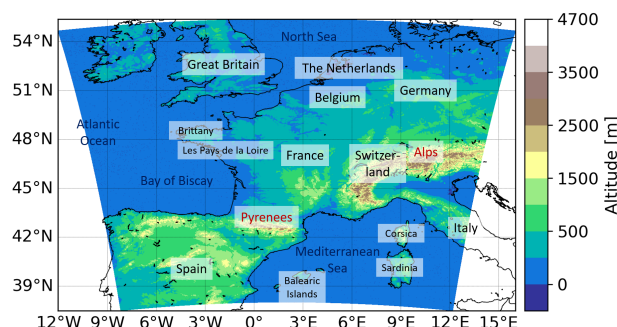
Figure 1. AROME-France physical domain and model topography. The AROME-France horizontal grid is equidistant at $1.3\,\mathrm{km}$ resolution.

Then, our LDA method and the model experiments are explained in Sections 5 and 6. Section 7 describe the AROME-France analysis resulting from LDA. One of four case studies is detailed using different assimilation experiments, among others the new LDA. Finally, Section 8 concludes this work.

2 Model configuration

AROME-France is the convective-scale, limited-area model run operationally by Météo-France since 2008 (Seity et al., 2011). It provides 36 to 42-hour forecasts five times a day (00 UTC, 03 UTC, 06 UTC, 12 UTC, 18 UTC). After an update in 2015, the model grid comprises 1440×1536 grid points in the horizontal with uniform $1.3\,\mathrm{km}$ horizontal resolution. The physical model domain and model topography are shown in Figure 1. In the vertical, the lowest model level is situated at around $5\,\mathrm{m}$ above ground. Each column reaches up to the highest level at $10\,\mathrm{hPa}$. The vertical resolution is refined homogeneously from top to bottom by a factor of 1.5. In total, 90 vertical levels (33 levels below $2000\,\mathrm{m}$) are computed. Model time steps equal $50\,\mathrm{s}$. Model dynamics are non-hydrostatic, semi-implicit, and semi-Lagrangian. Lateral boundary conditions (LBCs) are extracted from the global model ARPEGE (Bouyssel et al., 2022). AROME-France features a Davies relaxation (Davies, 1976) coupling and ARPEGE synchronization. The initial conditions rely on a 3DVar data assimilation technique (section Section 5).

Deep convection is expected to be mostly resolved on the model grid (Fischer et al., 2018). Parametrization of sub-grid scale shallow convection is based on Pergaud et al. (2009). AROME-France uses a mixed-phase microphysical scheme with riming processes and graupel (Seity et al., 2011). In particular, the microphysics scheme of AROME-France separates five prognostic hydrometeor variables, that are specific contents of precipitating species rain (q_r), snow (q_s), and graupel (q_g) and the two non-precipitating species ice crystals (q_i) and cloud droplets (q_c). In addition, the water vapor specific content q_v (also termed specific humidity) is computed. Hail is assumed to behave as large graupel particles. Overall, more than 25 processes are parametrized into the microphysics scheme (Lascaux et al., 2006). AROME-France physics include a 1-dimensional (1D) turbulence parametrization as combination of a prognostic turbulent kinetic energy (TKE) equation with a diagnostic mixing length. An Externalized Surface (SURFEX) scheme and the European Center for Medium-Range Weather Forecasts (ECMWF)

radiation parametrization are other components of AROME-France model physics. Details can be found in Seity et al. (2011);
150   Brousseau et al. (2016).

3   Lightning data

This work adapts the GEO lightning pseudo-observation generator as developed by Erdmann et al. (2022). It was trained using
low frequency (LF) ground-based National Lightning Detection Network (NLDN) records collected over the South-East US.
The LF ground-based lightning observations in this study are provided by the French network Meteorage (Schulz et al., 2016;
155   Pédeboy, 2015) as input. Meteorage locates total lightning with a separation of CG strokes and IC pulses. They are clustered to
the flash level data using the same method as Erdmann et al. (2020), i.e., a spatiotemporal clustering with criteria of $20\,\mathrm{km}$ and
$0.4\,\mathrm{s}$. To verify Meteorage data as suitable input to the generator, Meteorage and NLDN observations were compared to space-
borne ISS-LIS data as common reference (Erdmann, 2020): The flash detection effiency (DE) of NLDN relative to ISS-LIS was
about $76\,\%$. ISS-LIS detected about $59\,\%$ of the NLDN flashes. In France, Meteorage flash DE relative to ISS-LIS was about
160   $83\,\%$ while ISS-LIS detected about $57\,\%$ of the Meteorage flashes. The statistical evaluation of general flash characteristics
revealed that NLDN and Meteorage flashes feature similar distributions of flash extent (average of about $7.0\,\mathrm{km}$), flash duration
(average of about $0.2\,\mathrm{s}$), stroke/pulse number per flash (average of about 3.6). Meteorage, with shorter baseline distance than
NLDN, recorded on average higher LF currents for the occurring flashes (average of $9.5\,\mathrm{kA}$ and $8.3\,\mathrm{kA}$ for Meteorage and
NLDN, respectively). In all cases, large extent, long duration, as well as flashes with high number of events and strokes/pulses
165   for ISS-LIS and the LF network, respectively, were more likely detected by the other LLS than the small, short duration flashes.
Overall, Meteorage was validated as a suitable source for the input to the GEO lightning pseudo-observation generator. Pseudo-
observations of MTG-LI are then generated on a regular latitude-longitude grid with average pixel resolution of $7\,\mathrm{km}$ which
approximates the expected MTG-LI resolution over France (personal communication Bartolomeo Viticchiè, 2020). FEDs are
calculated per 5-minute interval that can then be summed as needed for the assimilation. This work uses a 10-minute interval
170   of FED data in the LDA that is centered at the time of the analysis (as done by Fierro et al., 2016; Hu et al., 2020). The short
period around the analysis reduces displacement errors in the analysis. The domain is limited to 40°N to 51°N and 5.5°W to
10°E, which is inside the AROME-France physical model domain. The pseudo MTG-LI FED is referred to as FED observation
hereafter to avoid confusion with the pseudo-observations (POs) created by the 1DBay retrieval.

An example of simulated MTG-LI is provided in Figure 2(a) for the entire study domain, and Figure 2(b) zoomed on the FED
175   maximum on 09 Aug. 2018, 13:55 UTC to 14:00 UTC. The regular latitude-longitude grid of the FED is obvious. Figure 2
accumulates data of $5\,\mathrm{min}$, and the FED pixels have a constant size of about 0.0630° latitude and 0.0896° longitude that
corresponds to an average pixel size of $7\,\mathrm{km}$ times $7\,\mathrm{km}$ in the study domain.

Figure 2(c) shows the zoomed-in simulated FED and adds the Meteorage CG strokes and IC pulses that were used as input for
the GEO lightning pseudo-observation generator. The vast majority of strokes and pulses lies within the area of strictly positive
180   FED. Figure 2(d) illustrates that the simulated MTG-LI flash centroids are situated within the corresponding Meteorage stroke
and pulse distribution.
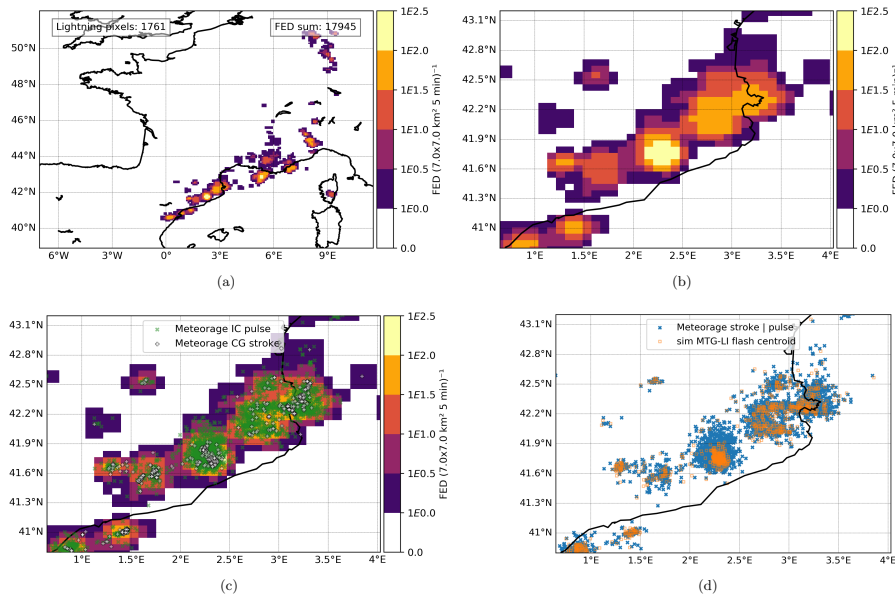
Figure 2. Simulated MTG-LI FED in the entire domain (a) and zoomed on the region of the maximum FED value (b) on $7\,\text{km} \times 7\,\text{km}$ grid. The Meteorage strokes and pulses that were used to generate the MTG-LI flashes are superimposed on the FED in (c). Simulated MTG-LI flash centroids and the corresponding Meteorage strokes+pulses in (d). Example for the period from 09 Aug. 2018, 13:55 UTC to 14:00 UTC.

4 Lightning observation operator

In consequence of the former studies (see Section 1), graupel mass appears to be a reliable proxy for lightning. Our observation operator is trained based on an observed relation between MTG-LI FED observations and 1-hour forecasts of AROME-France simulated graupel mass (m_g) for 24 days in 2018, i.e., 2 days each month. FED time periods of $10\,\text{min}$ are used (like, e.g., Fierro et al., 2016; Hu et al., 2020) centered at the corresponding time of the AROME-France analysis. The m_g profile is extracted from the AROME-France grid point closest to the FED pixel center. Thus, one specific m_g profile is related to one FED value. Following Deierling et al. (2008), column integrated graupel mass is taken for layers where the temperature was below $-5\,°\text{C}$. As a reminder, AROME-France graupel mass combines graupel and hail. All FED and column graupel mass values are further processed as climatological distributions (see Figure 3) without observation location and time. This approach is different from Deierling et al. (2008); Barthe et al. (2010) who used storm-based relationships of case studies, and from McCaul et al. (2009) who used the domain-wide peak values. Pixel-to-pixel m_g and FED were barely correlated in our study, with about 0.09 Pearson correlation coefficient, likely as a consequence of a typical displacement of convection in the model by more than the FED spatial resolution of $7\,\text{km}$. The second approach with domain-wide peak values was not further tested as it reduces the sample size for a regression analysis drastically. Our observation operator uses a simple linear regression between observed FED and simulated column graupel mass. It is unbiased by definition. Our approach optimizes both the slope factor and the y-intercept of the regression, whereas, e.g., McCaul et al. (2009) only used a proportionality between FED and a proxy.
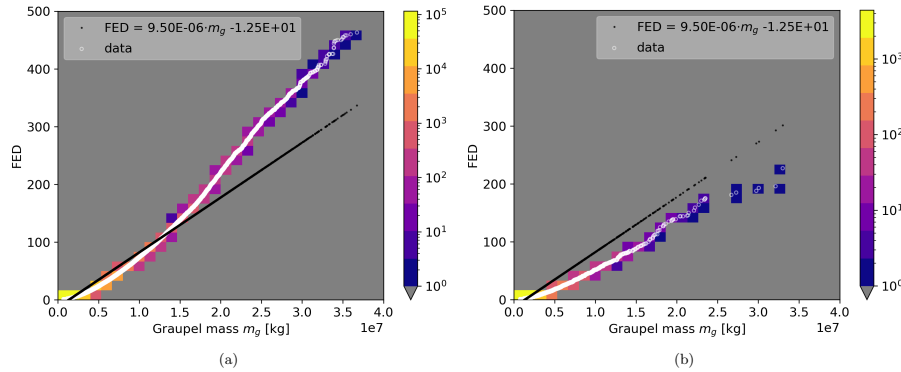
Figure 3. The observed FED, per $10\,\text{min}$ and on $7\,\text{km} \times 7\,\text{km}$ pixels, climatological distribution versus the climatological distribution of AROME-France graupel mass m_g at model grid points closest to each FED observation. Grid points with any of FED or m_g equal to zero are not considered. (a) shows the training of a linear regression for 24 days in 2018, and (b) shows the results of a validation for independent data of 2 additional days in 2018. Colors indicate the number of samples, the white points plot the data points, and black points applied the m_g values in the linear regression equation (see Figure legend).

Figure 3 presents the analyzed linear relationship between FED and column integrated graupel mass m_g that are calculated per $7\,\text{km} \times 7\,\text{km}$ pixel whereby m_g uses a single model grid point closest to the FED pixel center. It should be noted that all pixels with either FED equal to zero or m_g equal to zero are removed from the data. The observation operator represents the cases when lightning was actually observed. The training data (24 days) results are shown in Figure 3(a) and the results for 06 and 07 October 2018 as validation period can be seen in Figure 3(b). The Pearson correlation coefficient equals 0.97 for the training data and 0.92 for the validation data (0.96 combined).

Analyzing the training data, the linear relationship fits the majority of the data well. A discrepancy is identified for the largest graupel mass and FED values (Figure 3). Here, the observation operator tends to underestimate the FED for a given graupel mass. The high values (of both FED and graupel mass) are rare relative to the lower values as indicated by the colored pixels in Figure 3(a). Hence, this observed discrepancy litte affects the Pearson correlation coefficient. It should still be considered that high FED values are systematically underestimated. It is further noted that the y-intercept is negative, meaning that statistically a certain mass of graupel is required to get the first lightning. This result is well in accordance with the widely accepted non-inductive charging as main electrification process in extratropical storms.

The validation data (Figure 3(b)) follow roughly the regression line inferred from the training data. One can see, however, that the slope is smaller than that of the black regression line, i.e., the values of FED are always lower for a given m_g than the training data implies. The number of FED-m_g-pairs is significantly lower for the 48-hour validation case than for the 24-day training dataset. Furthermore, the validation data comprises one single meteorological situation, while the training data includes several weather situations in different seasons. The observed discrepancy is considered during the evaluation of results.

5 1DBay+3DVar assimilation method

The observation operator described in the previous section is used in the new lightning data assimilation method. Unlike Fierro et al. (2019); Hu et al. (2020) and others who used an empirical method to adjust moisture in thunderst[...], the expected water vapor PO is retrieved for each model grid column (applying Bayes' Theorem) in a 1DBay approach. This allows to i)

220 replace the humidity field in spurious convection areas with that of their convection-free environment, and thus in principle abolish the wet bias that results from data assimilation techniques that only consider the occurrence of lightning (e.g., Fierro et al., 2012, 2019; Hu et al., 2020), and ii) make use of the FED value to modulate the humidity field in observed lightning areas by leveraging the model's ability to create consistent, flow-dependent humidity and graupel profiles near the observation. Technically speaking, synthetic profiles are created and assimilated as sounding data.

225 The 1DBay retrieval of POs of relative humidity RH, $y_{\mathrm{po}}^{\mathrm{RH}}$, is defined as

$$y_{\mathrm{po}}^{\mathrm{RH}} = \sum_i x_i^{\mathrm{RH}} \frac{W_i}{\sum_j W_j} \tag{1}$$

with the weights W_i for each point as

$$W_i = \exp\left\{ -\frac{1}{2} \frac{[\mathrm{FED} - \mathrm{FFO}(x_i)]^2}{\sigma_o^2} \right\} \tag{2}$$

where i, j are counters for the grid points within the defined area, referred to as vicinity, and FFO means the FED forward

230 operator as specific observation operator. $\mathrm{FFO}(x_i)$ then defines the simulated AROME-France FED.

Equations (1) and (2) can be used with different model variables or diagnostics, e.g., the sensitivity test for σ_o as described in the following used x_i^{FED} rather than x_i^{RH}.

Each RH PO is the best estimation from a weighted linear combination of RH profiles taken from the model background in the vicinity of the FED observation.

235 The method was proposed by Caumont et al. (2010), used in the operational model AROME-France (Wattrelot et al., 2014), and applied by Borderies et al. (2019) for radar reflectivity data, and Duruisseau et al. (2019) for microwave radiances. Here, weights are calculated based on differences between observed and simulated FED. The 1DBay retrieves the best estimation of RH at the center of each observed FED pixel from the background using Bayes' Theorem. It is expected that the model can predict a quantity similar to the observation within a certain area in most cases. The vicinity is initially fixed to a square of

240 $160\,\mathrm{km} \times 160\,\mathrm{km}$ centered at the observation. This size follows the suggestion of Borderies et al. (2018, 2019). However, the FED pixels (about $7\,\mathrm{km}$) are significantly larger than the radar reflectivity pixels (about $1\,\mathrm{km}$) and a given vicinity contains less FED than radar datapoints to retrieve the expected profile. Hence, the vicinity is adapted to the specifications of the FED data. 1DBay vicinities of $160\,\mathrm{km}$, $320\,\mathrm{km}$, and $500\,\mathrm{km}$ were tested regarding the RMSE between observed FED and retrieved FED (not shown). It was found that larger vicinities give lower overall RMSE as there are more background profiles to feed

245 the retrieval and to find grid points that are similar to the FED observation. In consequence, all LDA experiments presented in the following use a 1DBay vicinity of $500\,\mathrm{km}$.

The database comprises model forecasts at the observation time and in the vicinity of the observation location. The covariance matrix of observation and observation operator is chosen diagonal with a trace of $n \cdot \sigma_o^2$, where n is the vertical dimension of the observations and equals 1 for the 2D variable FED. A small σ_o means that the retrieval favors columns with values close

250 to the FED observation. This can produce accurate retrievals; however, no retrieval can be created when the difference between all simulated FED in the vicinity and the observed FED is large relative to σ_o (see Equation (2) where weights approximate 0 in that case). Large values of σ_o cause smoothing over all grid points in the vicinity of the observation. In that case, the likelihood to retrieve POs is high, at the cost of a less accurate retrieval potentially independent of the observation.

The value for the standard deviation σ_o of the observation and observation operator is inferred from a sensitivity study. It

255 aims at minimizing the root mean square error (RMSE) between observed and retrieved pseudo FED for the 24 training days also used in Section 4. Pixel-to-pixel RMSE is used for all non-zero FED pixels and 10-minute FED intervals centered at each full hour. The pseudo FED is computed from joint use of the observation operator and the 1DBay retrieval. All FED values areF transformed to units of dB as $10 \cdot \log_{10}(\text{FED}/(7\,\text{km} \times 7\,\text{km}\ 10\,\text{min})^{-1})$ to account for the large range of scales, referred to as dBFED. FED equal to zero is transformed to dBFED of $-10\,\text{dB}$. In general, dBFED below $0\,\text{dB}$ means linear FED less than

260 $1\ (7\,\text{km} \times 7\,\text{km}\ 10\,\text{min})^{-1}$[1], i.e., no lightning activity. Figure 4(a) shows the curve of the RMSE between dBFED observation (from pseudo MTG-LI) and retrieved pseudo dBFED from the 1DBay retrieval for different σ_o. The RMSE between AROME-France background dBFED (AROME_dBFED), that was obtained from the observation operator without additional 1DBay, is shown as reference. Including the 1DBay retrieval (blue curve in Figure 4(a)) produces pseudo dBFED much closer to the dBFED observation, i.e., lower RMSE, than the AROME_dBFED (orange curve in Figure 4(a)). The minimum RMSE for the

265 retrieval is found at σ_o of $2.0\,\text{dB}$. This value is used for retrieving the pseudo-RH profiles in the following.

Case studies of fields of observed, background, and retrieved dBFED are conducted to visualize the effect of σ_o on the pseudo dBFED. One example of a 07 Oct. 2018, 00:00 UTC case is presented in Figure 4(b-d). The dBFED observation in Figure 4(b) shows lightning activity mainly in the south center of the domain. AROME_dBFED (Figure 4c) of the background exhibits positive dBFED in the region of dBFED observation, however, also widespread near the center of the domain and

270 over western France. The 2D distribution of the 1DBay retrieved pseudo dBFED in Figure 4(d) demonstrates that the method effectively reduces the spurious dBFED in these regions (retrieved dBFED below 0, grey and marine blue). In some regions, the 1DBay retrieves profiles to completely remove the spurious lightning, e.g., over western France and for some grid points over Switzerland. Spurious high values of AROME_dBFED near the center of the domain (Figure 4c) are effectively decreased to negative dBFED (marine blue in Figure 4d) meaning eventually no lightning activity, similar to the observation in that region

275 (Figure 4b). Furthermore, the pseudo dBFED values and areas of positive pseudo dBFED in the south center of the domain closely match the dBFED observation. The observed, shallow dBFED in northwestern Italy, to the north of Corsica, could not be reproduced by the 1DBay retrieval as the background does not provide any positive dBFED in the vicinity around this regional area.

An additional method, the humidity adjustment (HA), is applied if lightning (i.e., positive FED) is observed but all back-

280 ground FED values in the vicinity are zero. In this case, there is no estimated profile at this point and all W_i in the vicinity

---

[1]Non-integer FED values are possible when applying the observation operator.
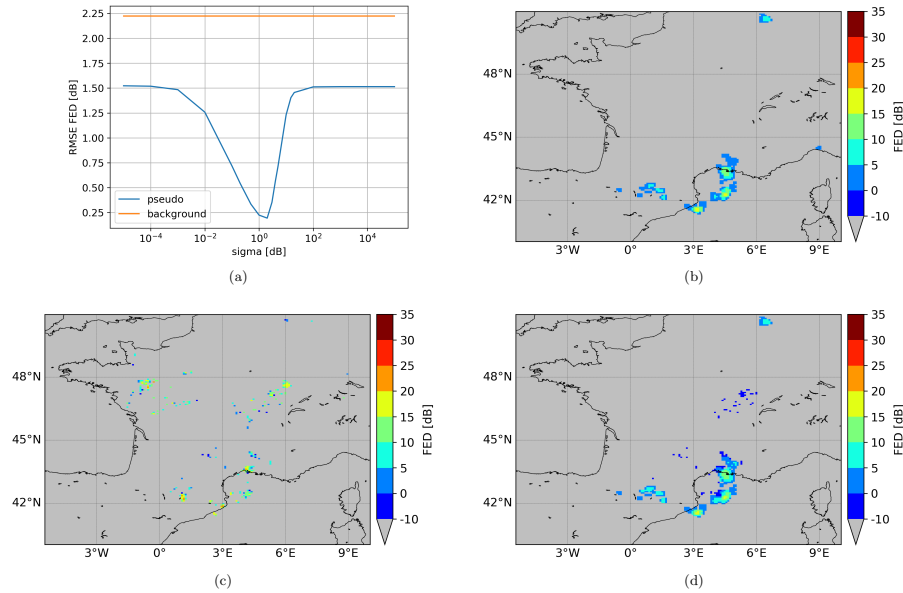
Figure 4. (a) The sensitivity test for standard deviation σ_o of the 1DBay retrieval as inferred from the pixel-to-pixel RMSE between the dBFED observation and the AROME_dBFED (background) as well as the 1DBay retrieved pseudo dBFED (pseudo). 07 Oct. 2018, 00:00 UTC, case with the MTG-LI dBFED observation (b), the model background AROME_dBFED (c), and the 1DBay retrieved pseudo dBFED with a σ_o of 2 (d). Grey color means no lightning in general.

equal zero. The HA is also applied if all background dBFED values within the vicinity of the FED observation are at least $10\,\mathrm{dB}$ smaller than the observed dBFED value. Although the sum of W_i can become greater than zero in this case, the retrieval would generate a profile that is too dry with respect to the FED observation. To produce RH POs, the layer between lifted condensation level (LCL) and $13\,\mathrm{km}$ is saturated (i.e., RH set to $100\,\%$) at all levels where the modeled RH is less than $100\,\%$. This is conceptually similar to the method of among others Fierro et al. (2019). However, the HA is only applied for few pseudo-RH profiles where the 1DBay method did not retrieve POs.

Another case with Equations (1) and (2) equal to 0 for all weights may occur if the observed FED equals 0 and the background FED is positive for all grid points in its vicinity. This behavior was observed for the initial 160-km vicinity, but not within the 320-km and 500-km vicinity. Thus, if the vicinity has a sufficient size, there are background grid points without lightning activity that can be used in the 1DBay retrieval. If, however, the vicinity is too small, one would need to remove spurious FED, i.e.convection and humidity from the model artificially.

Eventually, no pseudo-RH profiles are created if both the observed FED and the closest (in space) AROME-France background FED equal zero.

It should be mentioned that the 1DBay retrieval method has been initially developed and applied to retrieve humidity and cloud profiles from passive and active remote sensing data (e.g., Olson et al., 1996; Kummerow et al., 2001). Caumont et al. (2010) brought this approach forward by restricting the 1DBay method to use model profiles at the forecast time and in the

neighborhood of the observation. This approach was successfully applied by Wattrelot et al. (2014); Borderies et al. (2019) for radar reflectivity assimilation in AROME-France. However, a 1DBay has not yet been used to retrieve humidity profiles from FED data. Whereas an FED greater than zero is always related to the presence of graupel and thus a RH profile with a 300 cloud, an FED equal to zero does not necessarily mean a location without cloud coverage. It is the same problem which is faced for radar reflectivity, but presumably more marked than for the centimeter wavelength radars (Caumont et al., 2010) and even more than for the millimeter wavelength radars which are even more sensitive to the small hydrometeors (Borderies et al., 2019). In addition, FED is a 2D variable without vertical extent while the 1DBay retrieves vertical RH profiles. The use of integrated column graupel mass as proxy addresses the latter aspect by converting the 3D AROME-France products in a 2D 305 variable comparable to FED.

The retrieved pseudo-RH profiles are assimilated as sounding data in the 3DVar assimilation system of AROME-France. AROME-France uses a one-hour assimilation window. The short assimilation cycles aim at partially overcoming the missing temporal dimension and at allowing an assimilation of more high-frequency observations that can improve the initial conditions especially on the convective scale. AROME-France operationally assimilates surface (e.g., ground-stations, ships, buoys) and 310 aircraft measurements, Global Positioning System (GPS) Zenith Tropospheric Delay (ZTD) data, satellite brightness temperatures of several polar orbiting satellites and from Meteosat Second Generation (MSG) SEVIRI, satellite-based atmospheric motion vectors, and radar velocity and reflectivity data (Seity et al., 2011; Brousseau et al., 2016). The control variables temperature, specific humidity, surface pressure, and horizontal wind components. The 3DVar system minimizes a classical 3DVar cost function J of the state vector x:

$$315 \quad J(x) = \frac{1}{2}(x - x_b)^T \mathbf{B}^{-1}(x - x_b) + \frac{1}{2}[y_o - H(x)]^T \mathbf{R}^{-1}[y_o - H(x)] \qquad (3)$$

with the state vector of the background x_b, the observation vector y_o, the observation operator H, and the observation error covariance matrix $\mathbf{R}$. The climatological background error covariance matrix $\mathbf{B}$ is inferred from offline AROME-France ensemble assimilation as a multivariate set of calculations for the control variable covariances and cross-covariances (Brousseau et al., 2014).

320 6 Model simulation experiments

This section evaluates the effect of LDA relative to RDA. Since the application of the 1DBay retrieval for FED data constitutes a new approach, different experiments of AROME-France with respect to LDA are conducted. All experiments are initiated at 0000 UTC and run for a forecast period of 30 hours until 0600 UTC the following day.

Table 1 lists the six different assimilation experiments. First, there is a control experiment used as reference without RDA, 325 without Doppler wind velocity assimilation, and without LDA. It is called *CTRL*. The second experiment includes the use of radar data and is similar to the current operational AROME-France. It is referred to as *RDA*. All RDA experiments shown here assimilate both reflectivity and Doppler wind velocity.

While analyzing first LDA experiments, it was evident that the use of all FED observations leads to wrong results, i.e., the changes to the AROME-France background humidity contradicted the assimilated pseudo-RH profiles (not shown). This

Table 1. Simulation and assimilation techniques of the different AROME-France experiments conducted. They differ by the use of radar data assimilation (RDA) and lightning data assimilation (LDA), as well as the application of the *noCloud*(nC)-filter as described in the text.

Experiment	Assimilation	*noCloud*-filter
R (CTRL)	Reference (control)	no
RDA	CTRL + RDA	no
LDA	CTRL + LDA	no
LDAnC	CTRL + LDA	yes
RDA_LDA	CTRL + RDA + LDA	no
RDA_LDAnC	CTRL + RDA + LDA	yes

330 behavior is known to occur because the **R** matrix is diagonal whereas observation error cross-correlations are actually present, which leads to sub-optimal solutions (e.g., Rabier, 2006). It could be mitigated by reducing the number of assimilated observations (*thinning* Järvinen and Undén, 1997). This work thinned FED by a factor of 2 in latitude direction, i.e., 1 of 4 observations are assimilated, so that no observations of adjacent FED pixels are used. Tests revealed that this thinning was sufficient to eliminate the FED observation error correlations. For comparison, 1 of 64 radar observations, with a higher horizontal resolution than this FED data, are assimilated in AROME-France (Michel, 2018). The thinning, thus, prevents from assimilating observa-

335 tions with correlated observation errors contradicting the assumption of a diagonal **R** matrix. The resulting LDA without RDA is labeled *LDA*.

The second LDA experiment without RDA ,*LDAnC*, adds a so-called *noCloud*-filter. This *noCloud*-filter is utilized for locations where the observed FED equals zero but the AROME_FED exhibits lightning activity. Then, the distance to the

340 closest positive FED observation, d_{FED}, is computed. If d_{FED} remains within $21\,\mathrm{km}$, i.e., a maximum of three FED pixels, it is assumed that the profile is still situated within the same thundercloud being responsible for observed FED greater than zero. In this case, the RH profile of the background is kept to avoid reducing the RH if observed FED equals zero but the location is likely associated with a cloud. In the case where d_{FED} exceeds $21\,\mathrm{km}$, AROME-France profiles within $21\,\mathrm{km}$ are not considered in the 1DBay as they might belong to the spurious thunderclouds modeled but not observed. Hence, the

345 *noCloud*-filter should help to effectively reduce the background humidity for spurious convection.

The two remaining experiments combine both LDA methods with RDA. They are labeled *RDA_LDA* and *RDA_LDAnc*, respectively.

All model experiments are initiated one day prior to the start of the model forecast. During the first 24 hours, the 3DVar assimilation system of AROME-France creates 23 analyses (there is no analysis for the time of initialization). Therefore,

350 reference experiment, the LDA, and RDA are conducted for 23 hours in advance of the evaluated analysis. This time period is chosen as convection was observed within the model domain continuously. In addition, the long assimilation period allows AROME-France to well ingest the available observations.

7 The AROME-France analysis and forecast assimilating FED observations

This section describes the LDA ability to modify and update the model background. The following sections briefly introduce
355 the four test cases, detail one case, and discuss i) the LDA effects on the AROME-France background and ii) AROME-France
rainfall forecasts for this selected case. AROME-France simulations are mainly analyzed for the first 12 forecast hours since
the most effects of RDA and LDA are expected during these forecast hours, as seen in Fierro et al. (2019), for example, and
the influence of the lateral boundary conditions becomes predominant after 12 hours (Vié et al., 2011).

7.1 Case 1: 08 to 10 August 2018

360 Strong convection and lightning activity was observed over France on 07 Aug., and the electrical cells were still active over
northern France and Belgium during the early hours of 08 Aug. Moist and warm air created unstable conditions over south-
eastern France where lightning was observed during the entire day. Whereas a dominant southwest flow was present aloft,
winds in lower levels were calm but caused slight warm air advection. The 2-m temperatures reached up to $33\,°C$ while the
dew point temperatures exceeded $20\,°C$ over southwestern France. CAPE values far beyond $1000\,J\,kg^{-1}$ indicated potential
365 for widespread deep convection and thunderstorm activity. In the evening of 08 Aug., the major cold front associated with
the amplifying trough entered the study domain from the west. Strong convective cells formed over Spain and propagated all
the way over France to Belgium and western Germany following the air mass boundary and the eastward movement of the
trough. The storms left the study domain in the afternoon of 09 Aug. At that time, new cells formed over southeastern France
and remained quasi-stationary until the end of the day. Only few cells developed within the domain, i.e., over the northern
370 Mediterranean Sea, thereafter and until the end of the forecast period. The 30-hour forecast starts 09 Aug. 2018, 00:00 UTC,
preceded by a 24-hour period with hourly data assimilation.

7.1.1 AROME-France analysis

Details to create the AROME-France analysis are presented in Figure 5 for the model experiment *LDAnC* on 08 Aug. 2018,
23:00 UTC. The first row of the figure (a-c) includes the AROME_dBFED (a), the 1DBay dBFED (b), and the dBFED obser-
375 vation (c). AROME-France could not predict most of the lightning activity over the Bay of Biscay and southwestern France
(a and c; see Figure 1 for the locations of the regions of interest). The region of the highest observed dBFED is correctly
predicted, however, with underestimated dBFED values (Figure 5 a,b versus c). The 1DBay dBFED (Figure 5b) shows pos-
itive dBFED patterns that match the observed dBFED (Figure 5c) despite the fragmented dBFED in the AROME-France
background (Figure 5a). Hence, Figure 5(g) shows added IWV to the background in the regions where the AROME-France
380 background underestimates the dBFED. The 1DBay dBFED (Figure 5b) method retrieves profiles southern France (marine
blue) to reduce the spurious AROME_dBFED (Figure 5a versus c), implying that IWV should be reduced here. Consequently,
the PO IWV (Figure 5e) clearly decreases compared to the background IWV (Figure 5d) as shown with the difference between
PO IWV and background IWV (Figure 5g). In addition, the LDA experiment reduces the model IWV at rare locations where
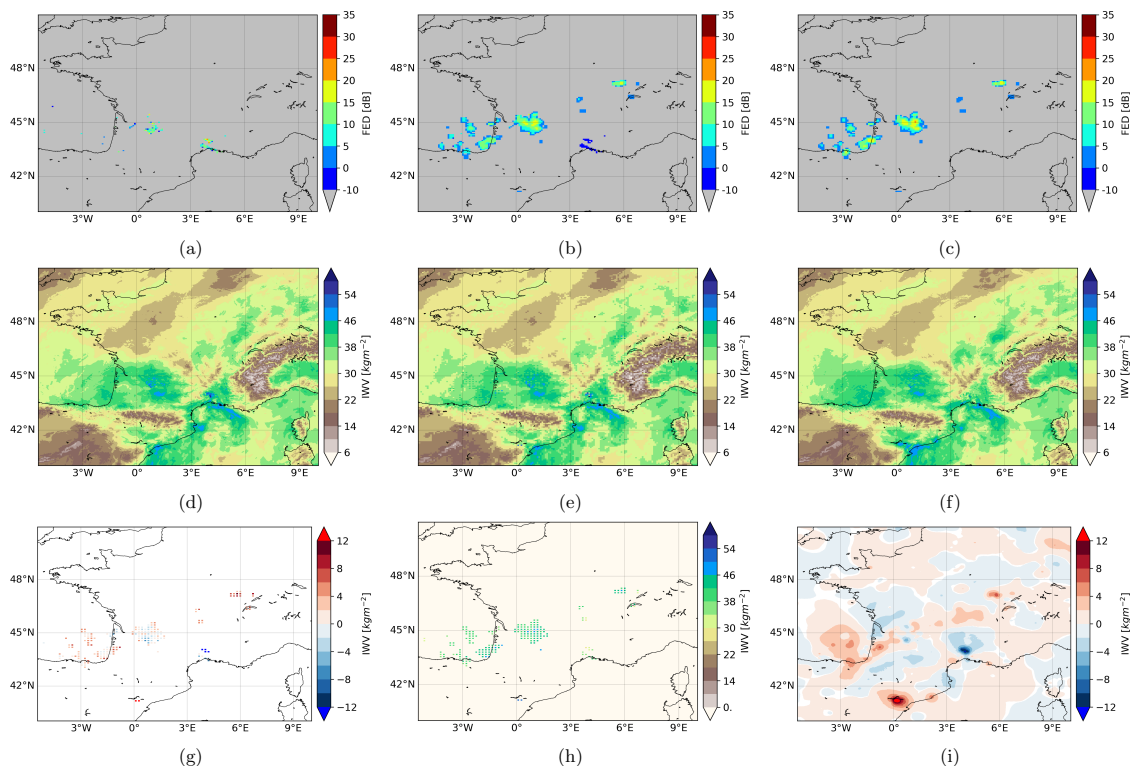
Figure 5. The background AROME_dBFED (a), the 1DBay retrieved dBFED (b), the MTG-LI dBFED observation (c), the AROME-France background IWV (d), PO IWV merged with the background where no profiles where retrieved (e), the IWV of the analysis (f), the difference between the PO IWV minus the background IWV (g), and the pure PO IWV including only points where RH was retrieved (h), and the difference in IWV of analysis and background (i). Results for 08 Aug. 2018, 23:00 UTC and model experiment *LDAnC*.

the AROME_dBFED exceeded the observed dBFED, e.g., due to a slight spatial shift of the local dBFED maxima at about

385   44.3°N and 0.8°E (compare Figure 5a,c and g at this location).

The 1DBay method aims at finding the profiles that should lead to an analysis with the expected increase and decrease of IWV relative to the observed and background dBFED values. Indeed, the analysis (Figure 5f) adds humidity to the background over the southwestern regions and for the cell over eastern France, as it can also be seen in the difference between analysis IWV and background IWV (Figure 5i) where LDA reduces model IWV where spurious lightning activity was predicted Figure 5(h)

390   shows in addition the IWV as output of the 1DBay retrieval method where no background IWV is included. At pixels with retrieved pseudo-RH profiles (positive values in panel h), the 1DBay-only IWV equals the PO IWV for most pixels. As IWV integrates the water vapor content per column, this finding means that the 1DBay method retrieves mostly complete vertical profiles. At pixels where 1DBay-only IWV values in Figure 5(h) would be smaller than the corresponding PO IWV values (Figure 5e) the HA method was used.

7.1.2 AROME-France rainfall forecasts

The *Antilope* rainfall accumulation (RA) combines the data of the operational radar network of Météo-France and ground-based rain gauges on a $0.01°$ resolution grid at each hour. RA maps of the first 6 hours are shown in Figure 6a to d for *Antilope*(a) and the experiments *RDA* (b), *LDA* (c) and *LDAnC* (d).

Three major thunderstorm tracks, labeled 1 to 3 from north to south hereafter, produced the bands of high RAs over the northwestern part of the domain (Figure 6a). The local maximum with very high RA up to $150\,\mathrm{mm}$ per 6 hours over southern France was caused by a quasi-stationary thunderstorm development. All three shown AROME-France experiments (Figure 6b-d) predicted the RA of track 1 relatively well. The two LDA experiments underestimated the area of high RA in the northwest of the domain for track 1. Experiments *RDA* and *LDA* overestimated the maximum RA over this region by about $20\,\mathrm{mm}$ and $5\,\mathrm{mm}$, respectively. Track 2 is best predicted by experiment *LDA* (Figure 6c), with good agreement in maximum RA and area of high RAs to the observation (Figure 6a). Experiment *LDAnC* (Figure 6d) could also predict the extent of the RAs related to track 2, but underestimated the RA amounts especially for the northern part of the track, i.e., most recent storm location to the prediction time. The experiment using RDA without LDA poorly predicts RA related to track 2. It is not totally clear whether the storm was modeled at all or placed too far south, however, the high RAs of track 2 were barely predicted. RAs of track 3 were similarly predicted by the three shown AROME-France experiments that all underestimate the RA of the southern part, i.e., during the beginning of the forecast period, and overestimate the RA of the northern part of the track, i.e., the most recent RA. 6-hour RAs related to the local thunderstorm over southern France were best predicted by *RDA*. Both LDA experiments somewhat underestimated the local RA maximum and the area of high RAs. In addition, the LDA experiment produces a spurious, local high RA cluster over northeastern Spain.

7.1.3 Evaluating the skill of AROME-France rainfall forecats

This section compares the predicted 6-hour RAs of different AROME-France experiments (Table 1) and the observations. RA observations are compared to the AROME-France output. The forecast skill is quantified calculating Fractions Skill Scores (FSSs). The FSS was introduced by Roberts and Lean (2008): The FSS can be calculated as skill score from the mean squared
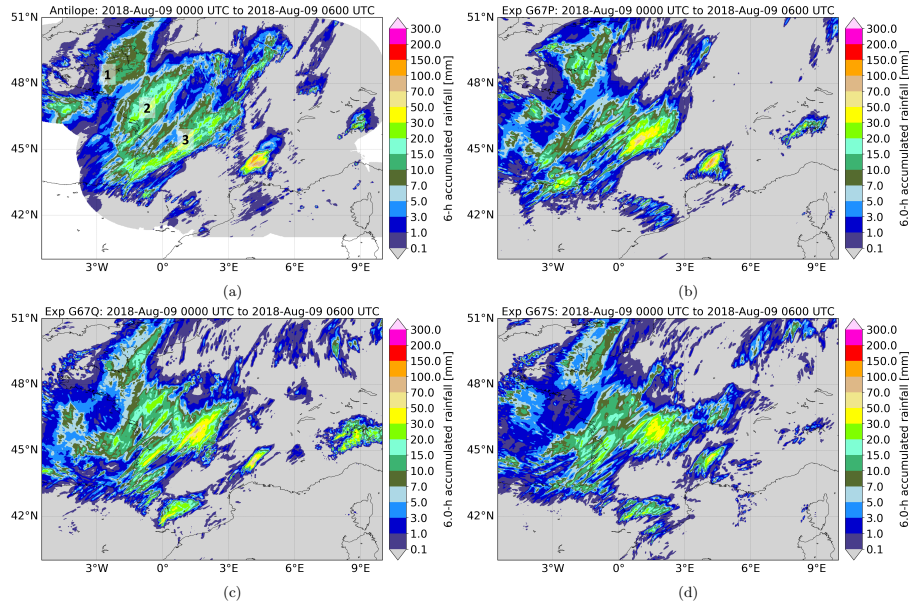
Figure 6. 6-hour rainfall accumulations (RAs) for the period until 09 Aug. 2018, 06:00 UTC, i.e., the first 6 forecast hours of the 30-hour forecast. RA observations (a), the AROME-France experiments *RDA* (b), *LDA* (c) and *LDAnC* (d). Three main thunderstorm tracks are labeled with black numbers in a.

error (MSE) for the observed and forecast fraction $O_{(n)}$ and $M_{(n)}$, respectively, from a neighborhood of length n as

$$\text{FSS}_{(n)} = 1 - \frac{\text{MSE}_{(n)}}{\text{MSE}_{(n)ref}}$$

with

$$\text{MSE}_{(n)} = \frac{1}{N_x N_y} \sum_{i=1}^{N_x} \sum_{j=1}^{N_y} \left[O_{(n)i,j} - M_{(n)i,j} \right]^2$$

$$\text{MSE}_{(n)ref} = \frac{1}{N_x N_y} \left[\sum_{i=1}^{N_x} \sum_{j=1}^{N_y} O^2_{(n)i,j} + \sum_{i=1}^{N_x} \sum_{j=1}^{N_y} M^2_{(n)i,j} \right]$$

and

$$O_{(n)i,j} = \frac{1}{n^2} \sum_{k=1}^{n} \sum_{l=1}^{n} I_O \left[i + k - 1 - \frac{n-1}{2}, j + l - 1 - \frac{n-1}{2} \right]^2$$

$$M_{(n)i,j} = \frac{1}{n^2} \sum_{k=1}^{n} \sum_{l=1}^{n} I_M \left[i + k - 1 - \frac{n-1}{2}, j + l - 1 - \frac{n-1}{2} \right]^2$$

420 (4)

with the observation and forecast binary fields I_O and I_M that equal 0 if the field value is smaller than the threshold, and 1 in all other cases. Our implementation uses the fast calculation of FSS in Python as proposed by Faggian et al. (2015). The FSS
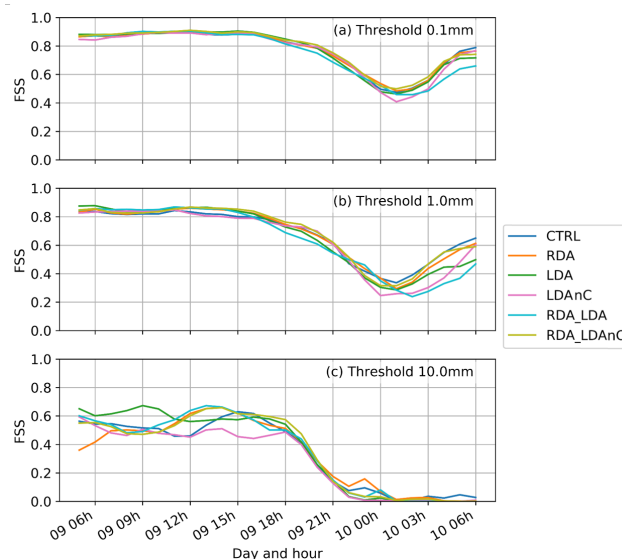
Figure 7. FSS for 6-hour RAs calculated hourly for a sliding window during the 30-hour forecast initiated 09 Aug., 00:00 UTC. The colors indicate the model experiments as defined in Section 6. 3 different RA thresholds are used, $0.1\,\mathrm{mm}$ (a), $1.0\,\mathrm{mm}$ (b), and $10.0\,\mathrm{mm}$ (c). The size of the domain used to calculate the FSS equals $0.5°$.

is calculated hourly for 6-hour RAs with a sliding 6-hour time window for the 30-hour forecast period. Forecasts are initiated at 00:00 UTC. It should be noted that the first FSS value of the time series includes the last hour of the assimilation window, 425 and ends at 05:00 UTC of the corresponding day.

Here, 6-hour RA thresholds of $0.1\,\mathrm{mm}$, $1.0\,\mathrm{mm}$, and $10.0\,\mathrm{mm}$ are used to represent different RA categories (weak, moderate, and strong rain). An FSS neighborhood of $0.5°$ is used. The figure shows the FSSs for the entire forecast period of 30 hours for the August case.

FSS of 0.8 to 0.9 for the RA thresholds $0.1\,\mathrm{mm}$ and $1.0\,\mathrm{mm}$ (Figure 7a and b, respectively) indicate that regions with 430 precipitation were equally well identified by all six conducted AROME-France experiments. The LDA without RDA and without the *noCloud*-filter,*LDA*, clearly outperforms all other experiments for the high RA threshold and during the first 10 hours of the forecast (Figure 7c). *RDA* exhibits the lowest FSS during the first 6 hours of the forecast due to the lack of high RAs of track 2 over *les Pays de la Loire* (see also Figure 6). The experiment *LDA* exhibits the highest FSS for the first 6 to 7 hours of the forecast demonstrating the high importance of lightning data for this case. Only after 12 hours of the forecast, the 435 combination of RDA and LDA, *RDA_LDA*, has the highest FSS so RDA gets more important the longer the forecast period.

This case study leads to the conclusion that the LDA without both RDA and the *noCloud*-filter of FED has the highest FSS to predict the heavy precipitation amounts. In that it differs from the other three case studies where the *noCloud*-filter mostly improves the LDA experiment skill. A future analysis might detail why the RDA and LDA with *noCloud*-filter have lower skill than the *LDA*. Such an analysis is beyond the present proof-of-concept scope.

Table 2. Summary of the 4 case studies.

Case	Dates (2018)	Weather conditions	Main precipitation source
1	08 to 10 Aug	instability, warm and moist low levels	deep convection, cold front
2	06 to 08 Oct	dissipating cyclone	cold front
3	01 to 03 Feb	trough and baroclinic wave	shallow convection, cold front
4	27 to 29 May	unstable conditions, low level moisture	deep convection, mesoscale system

7.2 Cases 2, 3, and 4

All case studies are summarized in Table 2. Besides the detailed case 1, the case studies analalyzed a cyclone with mainly frontal precipitation in autumn (case 2), shallow convection in cold early spring (case 3), and widespread deep convection in late spring (case 4). The evaluation of these three cases revealed that the RDA and LDA improve the RA forecast skill for convection within the study domain over western Europe. The combination of RDA and LDA exhibits always skill between RDA and LDA while once *RDA* and once *LDAnC* provided the best RA forecast. The best trade-off is found for the experiments using both RDA and LDA overall. In the future, a coupled assimilation of RDA and LDA could be tested. For example, PO RH profiles could be retrieved from a weighted product that includes both radar reflectivity and FED thereby adapting the 1DBay.

In situations, where convection from the Atlantic Ocean is advected into the study domain from the west, i.e., case 3, RDA and LDA could not improve the control run. Both RDA and LDA currently rely on ground-based observations with limited coverage over the Atlantic ocean. It is expected that the real MTG-LI observations will help to predict cloud systems forming over the ocean with higher efficiency than the LDA using the generated MTG-LI observations derived from ground-based observations.

8 Conclusions

The objective of this work is to design of an assimilation technique for the upcoming MTG-LI data for the regional, convection-permitting model AROME-France. To date, AROME-France applies a 3DVar assimilation system. A tailored 1DBay+3DVar assimilation technique (Caumont et al., 2010) is used to assimilate MTG-LI flash extent density (FED) in AROME-France. A similar assimilation technique is currently used operationally for radar reflectivity data assimilation in AROME-France, but has not yet been tested for the LDA.

This work first generated MTG-LI data that are used to create the FED observations (Erdmann et al., 2022). Then, an observation operator for FED is developed based on a linear, climatological relationship between observed FED and the column integrated AROME-France graupel mass above the $-5\,^\circ$C isotherm (m_g; as suggested by Deierling et al., 2008). The operator is trained for 24 days in 2018, and validated for 2 independent days in 2018. Pearson correlation coefficients of 0.97 and 0.92 for the training and validation data, respectively, reveal a very strong relation between the distributions of observed FED and model m_g. Nevertheless, the observation operator systematically overestimates the FED for m_g values greater than 1.5×10^7 kg per

465 AROME-France grid cell of $1.3\,\mathrm{km} \times 1.3\,\mathrm{km}$. More sophisticated observation operators are currently tested (Combarnous et al., 2022) but have not been included in this work yet.

The observation operator is then used to compare AROME-France-derived background FED (AROME_FED) to the FED observations. The 1DBay method identifies the best estimation of the FED from the background to in turn create pseudo-observations (POs) of RH-profiles based on both the FED observation and the AROME-France background fields. As back-
470 ground profiles are processed, the 1DBay method maintains model physics and flow characteristics.

The PO RH profiles add humidity to the AROME-France background where the observed FED exceeds the AROME_FED. It is further found that the 1DBay retrieval leads to reduction of humidity where the observed FED equals zero and the AROME_FED is positive, i.e., in regions of spurious convection with substantial m_g. Hence, the LDA technique improves the AROME-France background humidity. It is capable of both promoting convection in regions with lightning and suppress-
475 ing spurious convection. This was successfully verified in four case studies where the new LDA technique provided similar skill than the operational RDA in AROME-France.

FED exhibits the highest values near the convective core of a thunderstorm and the lightning activity does not always cover the entire cloud size. In fact, zero FED exists at cloudy locations. In order to address the specific nature of FED data, the 1DBay retrieval method is adapted. In detail, the vicinity used identify vertical profiles in the 1DBay method is expanded
480 and a so-called *noCloud*-filter is introduced. First results reveal that this adaption of the method can help to more effectively reduce the background humidity in regions of spurious convection, and to avoid a reduction of the background humidity if the profile occurs at the location of a cloud. Nonetheless, one of the four case studies revealed more skill in the LDA without the *noCloud*-filter than the LDA using this modification. The authors thus encourage further research on how the specifications of FED data can best be addressed by the LDA scheme, i.e., correlations between lightning locations and cloud cover.

485 In addition, this study found that thinning of the FED observations (on a grid of resolution of $7\,\mathrm{km}$) was necessary to avoid the effect of correlations between the observation errors that violates the assumptions of a diagonal observation error matrix in the AROME-France 3DVar data assimilation system (not shown).

Finally, 6-hour forecasts of RA fields are evaluated through FSS analysis. The developed LDA scheme can in general compete with the established radar data assimilation (RDA). Especially for the higher precipitation threshold of $10\,\mathrm{mm}$ per 6
490 hours, the LDAs exhibit higher FSSs during the first hours of the 30-hour forecast for two of four case studies. Positive effects on the forecast of rainfall by both RDA and LDA are found mainly for the high precipitation threshold and during the first 9 to 12 hours of the forecast. Longer forecast times show small spread in FSS between control run, RDA, and LDA for the three RA thresholds indicating that the assimilated radar and FED data do not significant effect the model forecast after 12 hours. The FSS of the combination of RDA and LDA indicate in most cases skill between the RDA and the LDA. In particular,
495 the combination does not gain the highest skill, meaning that either an LDA without RDA or an RDA without LDA can lead to more accurate rainfall forecasts. The combined RDA-LDA approach does, however, provide the best trade-off for the four different cases studied overall. The case of 02 February 2018 was unique in that neither RDA nor LDA improved the FSS of the control run. This case was significantly influenced by weather phenomena over the Atlantic Ocean, with limited radar

and Meteorage coverage. Real MTG-LI data will provide more accurate lightning records over the Atlantic than the synthetic

500 MTG-LI data based on Meteorage observations used in this study, and the LDA performance might improve in such situations.

It could be further studied whether the radar reflectivity and LDA can be coupled. A coupled approach may help to overcome some issues explained for zero FED at cloudy locations in general or at least for precipitating clouds, and, at the same time benefit from the successful promotion and suppression of convection by both RDA and LDA. As the LDA explorered here is based on satellite observations, such a coupled approach will also benefit to forecasts over regions with limited radar coverage.

505 The specific improvement over regions such as oceans and mountain ranges has not been studied here since our MTG-LI observations are based on ground-based Meteorage records. A study addressing in particular the skill over such regions would be of great interest as soon as real MTG-LI data become available.

Author contributions. FE wrote the paper text and created the figures. OC and ED were involved in content creation. All contributed to article reviews. OC and FE developed the assimilation technique.

510 *Competing interests.* The authors declare that they have no conflict of interest.

Acknowledgements. This work was a part of FE's PhD and as such funded by CNES and Météo-France. This article is funded by the SOLID (CNES) project and the EXAEDRE project (ANR-16-CE04-0005).

References

Allen, B. J., Mansell, E. R., Dowell, D. C., and Deierling, W.: Assimilation of Pseudo-GLM Data Using the Ensemble Kalman Filter, Monthly Weather Review, 144, 3465–3486, https://doi.org/10.1175/MWR-D-16-0117.1, 2016.

Apodaca, K., Zupanski, M., DeMaria, M., Knaff, J. A., and Grasso, L. D.: Development of a hybrid variational-ensemble data assimilation technique for observed lightning tested in a mesoscale model, Nonlin. Processes Geophys., 21, 1027–1041, https://doi.org/10.5194/npg-21-1027-2014, 2014.

Barthe, C., Deierling, W., and Barth, M. C.: Estimation of total lightning from various storm parameters: A cloud-resolving model study, Journal of Geophysical Research: Atmospheres, 115, https://doi.org/10.1029/2010JD014405, 2010.

Betz, H. D., Schmidt, K., Laroche, P., Blanchet, P., Oettinger, W. P., Defer, E., Dziewit, Z., and Konarski, J.: LINET—An international lightning detection network in Europe, Atmospheric Research, 91, 564 – 573, https://doi.org/https://doi.org/10.1016/j.atmosres.2008.06.012, 13th International Conference on Atmospheric Electricity, 2009.

Borderies, M., Caumont, O., Augros, C., Bresson, E., Delanoë, J., Ducrocq, V., Fourrié, N., Bastard, T. L., and Nuret, M.: Simulation of W-band radar reflectivity for model validation and data assimilation, Quarterly Journal of the Royal Meteorological Society, 144, 391–403, https://doi.org/10.1002/qj.3210, 2018.

Borderies, M., Caumont, O., Delanoë, J., Ducrocq, V., Fourrié, N., and Marquet, P.: Impact of airborne cloud radar reflectivity data assimilation on kilometre-scale numerical weather prediction analyses and forecasts of heavy precipitation events, Natural Hazards and Earth System Sciences, 19, 907–926, https://doi.org/10.5194/nhess-19-907-2019, 2019.

Bouyssel, F., Berre, L., Bénichou, H., Chambon, P., Girardot, N., Guidard, V., Loo, C., Mahfouf, J.-F., Moll, P., Payan, C., and Raspaud, D.: The 2020 Global Operational NWP Data Assimilation System at Météo-France, Data Assimilation for Atmospheric, Oceanic and Hydrologic Applications, IV, 645–664, https://doi.org/10.1007/978-3-030-77722-7_25, 2022.

Bovalo, C., Barthe, C., and Pinty, J.-P.: Examining relationships between cloud-resolving model parameters and total flash rates to generate lightning density maps, Quarterly Journal of the Royal Meteorological Society, 145, 1250–1266, https://doi.org/10.1002/qj.3494, 2019.

Brousseau, P., Desroziers, G., Bouttier, F., and Chapnik, B.: A posteriori diagnostics of the impact of observations on the AROME-France convective-scale data assimilation system, Quarterly Journal of the Royal Meteorological Society, 140, 982–994, https://doi.org/10.1002/qj.2179, 2014.

Brousseau, P., Seity, Y., Ricard, D., and Léger, J.: Improvement of the forecast of convective activity from the AROME-France system, Quarterly Journal of the Royal Meteorological Society, 142, 2231–2243, https://doi.org/10.1002/qj.2822, 2016.

Buiat, M., Porcu, F., and Dietrich, S.: Observing relationships between lightning and cloud profiles by means of a satellite-borne cloud radar, Atmospheric Measurement Techniques, 10, 221, https://doi.org/10.5194/amt-10-221-2017, 2017.

Caumont, O., Ducrocq, V., Wattrelot, E., Jaubert, G., and Pradier-Vabre, S.: 1D+3DVar assimilation of radar reflectivity data: a proof of concept, Tellus A: Dynamic Meteorology and Oceanography, 62, 173–187, https://doi.org/10.1111/j.1600-0870.2009.00430.x, 2010.

Chen, Y., Yu, Z., Han, W., He, J., and Chen, M.: Case Study of a Retrieval Method of 3D Proxy Reflectivity from FY-4A Lightning Data and Its Impact on the Assimilation and Forecasting for Severe Rainfall Storms, Remote Sensing, 12, 1165, https://doi.org/10.3390/rs12071165, 2020.

Combarnous, P., Erdmann, F., Caumont, O., Defer, E., and Martet, M.: An observation operator for geostationary lightning imager data assimilation in the French storm-scale numerical weather prediction system AROME, Natural Hazards and Earth System Sciences Discussions, 2022, 1–30, https://doi.org/10.5194/nhess-2022-39, 2022.

550 Davies, H. C.: A lateral boundary formulation for multi-level prediction models, Quarterly Journal of the Royal Meteorological Society, 102, 405–418, https://doi.org/10.1002/qj.49710243210, 1976.

Deierling, W. and Petersen, W. A.: Total lightning activity as an indicator of updraft characteristics, Journal of Geophysical Research, 113, D16 210, https://doi.org/10.1029/2007JD009598, 2008.

Deierling, W., Petersen, W. A., Lathman, J., Ellis, S., and Christian, H. J.: The relationship between lightning activity and ice fluxes in
555 thunderstorms, Journal of Geophysical Research, 113, D15 210, https://doi.org/10.1029/2007JD009700, 2008.

Dixon, K., Mass, C., Hakim, G., and Holzworth, R.: The Impact of Lightning Data Assimilation on Deterministic and Ensemble Forecasts of Convective Events, Journal of Atmospheric and Oceanic Technology, 33, https://doi.org/10.1175/JTECH-D-15-0188.1, 2016.

Dobber, M. and Grandell, J.: Meteosat Third Generation (MTG) Lightning Imager (LI) Instrument Performance and Calibration from User Perspective, in Proceedings of the 23rd Conference on Characterization and Radiometric Calibration for Remote Sensing (CALCON),
560 11-14 August 2014, Utah State University, Logan, Utah, USA. 13 pages, 2014.

Duruisseau, F., Chambon, P., Wattrelot, E., Barreyat, M., and Mahfouf, J.-F.: Assimilating cloudy and rainy microwave observations from SAPHIR on board Megha Tropiques within the ARPEGE global model, Quarterly Journal of the Royal Meteorological Society, 145, 620–641, https://doi.org/10.1002/qj.3456, 2019.

Erdmann, F.: Préparation à l'utilisation des observations de l'imageur d'éclairs de Météosat Troisième Génération pour la prévision
565 numérique à courte échéance (Preparation for the use of Meteosat Third Generation Lightning Imager observations in short-term numerical weather prediction), Ph.D. thesis, Université Toulouse 3 – Paul Sabatier, Toulouse, France, http://thesesups.ups-tlse.fr/4947/, 2020.

Erdmann, F., Defer, E., Caumont, O., Blakeslee, R. J., Pédeboy, S., and Coquillat, S.: Concurrent satellite and ground-based light-ning observations from the Optical Lightning Imaging Sensor (ISS-LIS), the low-frequency network Meteorage and the SAETTA
570 Lightning Mapping Array (LMA) in the northwestern Mediterranean region, Atmospheric Measurement Techniques, 13, 853–875, https://doi.org/10.5194/amt-13-853-2020, 2020.

Erdmann, F., Caumont, O., and Defer, E.: A geostationary lightning pseudo-observation generator utilizing low frequency ground-based lightning observations, Journal of Atmospheric and Oceanic Technology, 39, 3 – 30, https://doi.org/10.1175/JTECH-D-20-0160.1, 2022.

Faggian, N., Roux, B., Steinle, P., and Ebert, B.: Fast calculation of the Fractions Skill Score, Mausam, 66, 457–466, 2015.

575 Federico, S., Avolio, E., Petracca, M., Panegrossi, G., Sanò, P., Casella, D., and Dietrich, S.: Simulating lightning into the RAMS model: implementation and preliminary results, Natural Hazards and Earth System Sciences, 14, 2933–2950, https://doi.org/10.5194/nhess-14-2933-2014, 2014.

Federico, S., Panegrossi, G., Petracca, M., Transerici, C., and Dietrich, S.: Impact of the assimilation of lightning data on the precipitation forecast at different forecast ranges, Advances in Science and Research, 14, 187–194, https://doi.org/10.5194/asr-14-187-2017, 2017.

580 Fierro, A. O., Mansell, E. R., Ziegler, C. L., , and MacGorman, D. R.: Application of a Lightning Data Assimilation Technique in the WRF-ARW Model at Cloud-Resolving Scales for the Tornado Outbreak of 24 May 2011, Monthly Weather Review, 140, 2609–2627, https://doi.org/10.1175/MWR-D-11-00299.1, 2012.

Fierro, A. O., Gao, J., Ziegler, C. L., Mansell, E. R., MacGorman, D. R., and Dembrek, S. R.: Evaluation of a Cloud-Scale Lightning Data Assimilation Technique and a 3DVAR Method for the Analysis and Short-Term Forecast of the 29 June 2012 Derecho Event, Monthly
585 Weather Review, 142, 183–202, https://doi.org/10.1175/MWR-D-13-00142.1, 2014.

Fierro, A. O., Gao, J., Ziegler, C. L., Calhoun, K. M., Mansell, E. R., and MacGorman, D. R.: Assimilation of Flash Extent Data in the Variational Framework at Convection-Allowing Scales: Proof-of-Concept and Evaluation for the Short-Term Forecast of the 24 May 2011 Tornado Outbreak, Monthly Weather Review, 144, 4373–4393, https://doi.org/10.1175/MWR-D-16-0053.1, 2016.

Fierro, A. O., Wang, Y., Gao, J., and Mansell, E. R.: Variational Assimilation of Radar Data and GLM Lightning-Derived Water Vapor for the Short-Term Forecasts of High-Impact Convective Events, Monthly Weather Review, 147, 4045–4069, https://doi.org/10.1175/MWR-D-18-0421.1, 2019.

Fischer, C., Bouyssel, F., Brousseau, P., El Khatib, R., Pottier, P., Seity, Y., Wattrelot, E., and Joly, A.: Les modèles opérationnels de prévision numérique à aire limitée de Météo-France, La Météorologie, 100, 18–28, https://doi.org/10.4267/2042/65139, numéro Spécial Anniversaire 25 ans, 2018.

Formenton, M., Panegrossi, G., Casella, D., Dietrich, S., Mugnai, A., Sano, P., Di Paolo, F., Betz, H.-D., Price, C., and Yair, Y.: Using a cloud electrification model to study relationships between lightning activity and cloud microphysical structure, Natural Hazards and Earth System Sciences, 13, 1085–1104, https://doi.org/10.5194/nhess-13-1085-2013, 2013.

Giannaros, T. M., Kotroni, V., and Lagouvardos, K.: Predicting lightning activity in Greece with the Weather Research and Forecasting (WRF) model, Atmospheric Research, 156, 1 – 13, https://doi.org/https://doi.org/10.1016/j.atmosres.2014.12.009, 2015.

Giannaros, T. M., Kotroni, V., and Lagouvardos, K.: WRF-LTNGDA: A lightning data assimilation technique implemented in the WRF model for improving precipitation forecasts, Environmental Modelling & Software, 76, 54 – 68, https://doi.org/https://doi.org/10.1016/j.envsoft.2015.11.017, 2016.

Goodman, S. J., Blakeslee, R. J., Koshak, W. J., Mach, D., Bailey, J., Buechler, D., Carey, L., Schultz, C., Bateman, M., McCaul, E., and Stano, G.: The GOES-R Geostationary Lightning Mapper (GLM), Atmospheric Research, 125-126, 34 – 49, https://doi.org/https://doi.org/10.1016/j.atmosres.2013.01.006, 2013.

Hu, J., Fierro, A. O., Wang, Y., Gao, J., and Mansell, E. R.: Exploring the Assimilation of GLM-Derived Water Vapor Mass in a Cycled 3DVAR Framework for the Short-Term Forecasts of High-Impact Convective Events, Monthly Weather Review, 148, 1005–1028, https://doi.org/10.1175/MWR-D-19-0198.1, 2020.

Janisková, M. and Lopez, P.: Linearized Physics for Data Assimilation at ECMWF, in: Data Assimilation for Atmospheric, Oceanic and Hydrologic Applications, edited by Park, S. and Xu, L., vol. 2, Springer, Berlin, Heidelberg, https://doi.org/10.1007/978-3-642-35088-7_11, 2013.

Järvinen, H. and Undén, P.: Observation screening and background quality control in the ECMWF 3D-Var data assimilation system, Tech. rep. ECMWF, https://doi.org/10.21957/lyd3q81/, 1997.

Karagiannidis, A., Lagouvardos, K., Lykoudis, S., Kotroni, V., Giannaros, T., and Betz, H.-D.: Modeling lightning density using cloud top parameters, Atmospheric Research, 222, 163 – 171, https://doi.org/https://doi.org/10.1016/j.atmosres.2019.02.013, 2019.

Kong, R., Xue, M., Fierro, A. O., Jung, Y., Liu, C., Mansell, E. R., and MacGorman, D. R.: Assimilation of GOES-R Geostationary Lightning Mapper Flash Extent Density Data in GSI EnKF for the Analysis and Short-Term Forecast of a Mesoscale Convective System, Monthly Weather Review, 148, 2111–2133, https://doi.org/10.1175/MWR-D-19-0192.1, 2020.

Kummerow, C., Hong, Y., Olson, W. S., Yang, S., Adler, R. F., McCollum, J., Ferraro, R., Petty, G., Shin, D.-B., and Wilheit, T. T.: The Evolution of the Goddard Profiling Algorithm (GPROF) for Rainfall Estimation from Passive Microwave Sensors, Journal of Applied Meteorology, 40, 1801–1820, https://doi.org/10.1175/1520-0450(2001)040<1801:TEOTGP>2.0.CO;2, 2001.

Lagouvardos, K., Kotroni, V., Defer, E., and Bousquet, O.: Study of a heavy precipitation event over southern France, in the frame of HYMEX project: Observational analysis and model results using assimilation of lightning, Atmospheric Research, 134, 45 – 55, https://doi.org/https://doi.org/10.1016/j.atmosres.2013.07.003, 2013.

625 Lascaux, F., Richard, E., and Pinty, J.-P.: Numerical simulations of three different MAP IOPs and the associated microphysical processes, Quarterly Journal of the Royal Meteorological Society, 132, 1907–1926, https://doi.org/10.1256/qj.05.197, 2006.

Liu, P., Yang, Y., Gao, J., Wang, Y., and Wang, C.: An Approach for Assimilating FY4 Lightning and Cloud Top Height Data Using 3DVAR, Frontiers in Earth Science, 8, 288, https://doi.org/10.3389/feart.2020.00288, 2020.

Lynn, B. H., Kelman, G., and Ellrod, G.: An Evaluation of the Efficacy of Using Observed Lightning to Improve Convective Lightning
630 Forecasts, Weather and Forecasting, 30, 405–423, https://doi.org/10.1175/WAF-D-13-00028.1, 2015.

Mansell, E. R.: Storm-Scale Ensemble Kalman Filter Assimilation of Total Lightning Flash-Extent Data, Monthly Weather Review, 142, 3683–3695, https://doi.org/10.1175/MWR-D-14-00061.1, 2014.

Mansell, E. R., Ziegler, C. L., and MacGorman, D. R.: A Lightning Data Assimilation Technique for Mesoscale Forecast Models, Monthly Weather Review, 135, 1732–1748, https://doi.org/10.1175/MWR3387.1, 2007.

635 Marchand, M. R. and Fuelberg, H. E.: Assimilation of Lightning Data Using a Nudging Method Involving Low-Level Warming, Monthly Weather Review, 142, 4850–4871, https://doi.org/10.1175/MWR-D-14-00076.1, 2014.

McCaul, Eugene W., J., Goodman, S. J., LaCasse, K. M., and Cecil, D. J.: Forecasting Lightning Threat Using Cloud-Resolving Model Simulations, Weather and Forecasting, 24, 709–729, https://doi.org/10.1175/2008WAF2222152.1, 2009.

Michel, Y.: Revisiting Fisher's approach to the handling of horizontal spatial correlations of observation errors in a variational framework,
640 Quarterly Journal of the Royal Meteorological Society, 144, 2011–2025, https://doi.org/https://doi.org/10.1002/qj.3249, 2018.

Olson, W. S., Kummerow, C. D., Heymsfield, G. M., and Giglio, L.: A Method for Combined PassiveActive Microwave Retrievals of Cloud and Precipitation Profiles, Journal of Applied Meteorology, 35, 1763–1789, https://doi.org/10.1175/1520-0450(1996)035<1763:AMFCPM>2.0.CO;2, 1996.

Papadopoulos, A., Chronis, T., and Anagnostou, E.: Improving Convective Precipitation Forecasting through Assimilation of Regional Light-
645 ning Measurements in a Mesoscale Model, Monthly Weather Review, 133, 1961–1977, https://doi.org/10.1175/MWR2957.1, 2005.

Pergaud, J., Masson, V., Malardel, S., and Couvreux, F.: A Parameterization of Dry Thermals and Shallow Cumuli for Mesoscale Numerical Weather Prediction, Boundary-Layer Meteorology, 132, 83–106, https://doi.org/10.1007/s10546-009-9388-0, 2009.

Pessi, A. T. and Businger, S.: The Impact of Lightning Data Assimilation on a Winter Storm Simulation over the North Pacific Ocean, Monthly Weather Review, 137, 3177–3195, https://doi.org/10.1175/2009MWR2765.1, 2009.

650 Price, C. and Rind, D.: A simple lightning parameterization for calculating global lightning distributions, J. Geophys. Res., 97, 9919–9933, https://doi.org/10.1029/92JD00719, 1992.

Price, C. and Rind, D.: What determines the cloud-to-ground lightning fraction in thunderstorms?, Geophysical Research Letters, 20, 463–466, https://doi.org/10.1029/93GL00226, 1993.

Pédeboy, S.: Analysis of the French lightning locating system location accuracy, pp. 337–341, https://doi.org/10.1109/SIPDA.2015.7339299,
655 balneário Camboriú, Brazil, 28th Sept. to 2nd Oct. 2015, 2015.

Qie, X., Zhu, R., Yuan, T., Wu, X., Li, W., and Liu, D.: Application of total-lightning data assimilation in a mesoscale convective system based on the WRF model, Atmospheric Research, 145-146, 255 – 266, https://doi.org/https://doi.org/10.1016/j.atmosres.2014.04.012, 2014.

Rabier, F.: Importance of Data: A Meteorological Perspective, in: Ocean Weather Forecasting, edited by Chassignet, E. and Verron, J.,
chap. 12, pp. 343–360, Springer, Dordrecht, https://doi.org/10.1007/1-4020-4028-8_12, 2006.

Roberts, N. and Lean, H.: Scale-Selective Verification of Rainfall Accumulations from High-Resolution Forecasts of Convective Events,
Monthly Weather Review - MON WEATHER REV, 136, 78–97, https://doi.org/10.1175/2007MWR2123.1, 2008.

Schulz, W., Diendorfer, G., Pedeboy, S., and Poelman, D. R.: The European lightning location system EUCLID – Part 1: Performance
analysis and validation, Nat. Hazards Earth Syst. Sci., 16, 595–605, https://doi.org/10.5194/nhess-16-595-2016, 2016.

Seity, Y., Brousseau, P., Malardel, S., Hello, G., Bénard, P., Bouttier, F., Lac, C., and Masson, V.: The AROME-France Convective-Scale
Operational Model, Monthly Weather Review, 139, 976–991, https://doi.org/10.1175/2010MWR3425.1, 2011.

Vié, B., Nuissier, O., and Ducrocq, V.: Cloud-Resolving Ensemble Simulations of Mediterranean Heavy Precipitating Events: Uncertainty on
Initial Conditions and Lateral Boundary Conditions, Monthly Weather Review, 139, 403 – 423, https://doi.org/10.1175/2010MWR3487.1,
2011.

Wang, H., Liu, Y., Cheng, W. Y. Y., Zhao, T., Xu, M., Liu, Y., Shen, S., Calhoun, K. M., and Fierro, A. O.: Improving Lightning and
Precipitation Prediction of Severe Convection Using Lightning Data Assimilation With NCAR WRF-RTFDDA, Journal of Geophysical
Research: Atmospheres, 122, 12,296–12,316, https://doi.org/10.1002/2017JD027340, 2017a.

Wang, H., Liu, Y., Zhao, T., Liu, Y., Xu, M., Shen, S., Jiang, Y., Yang, H., and Feng, S.: Continuous Assimilation of Lightning Data Using
Time-Lagged Ensembles for a Convection-Allowing Numerical Weather Prediction Model, Journal of Geophysical Research: Atmo-
spheres, 123, 9652–9673, https://doi.org/10.1029/2018JD028494, 2018.

Wang, Y., Yang, Y., and Wang, C.: Improving forecasting of strong convection by assimilating cloud-to-ground lightning data using the
physical initialization method, Atmospheric Research, 150, 31 – 41, https://doi.org/https://doi.org/10.1016/j.atmosres.2014.06.017, 2014.

Wang, Y., Yang, Y., Liu, D., Zhang, D., Yao, W., and Wang, C.: A Case Study of Assimilating Lightning-Proxy Relative Humidity with
WRF-3DVAR, Atmosphere, 8, 20, https://doi.org/10.3390/atmos8030055, 2017b.

Wattrelot, E., Caumont, O., and Mahfouf, J.-F.: Operational Implementation of the 1D+3D-Var Assimilation Method of Radar Reflectivity
Data in the AROME Model, Monthly Weather Review, 142, 1852–1873, https://doi.org/10.1175/MWR-D-13-00230.1, 2014.

Wong, J., Barth, M. C., and Noone, D.: Evaluating a lightning parameterization based on cloud-top height for mesoscale numerical model
simulations, Geoscientific Model Development, 6, 429–443, https://doi.org/10.5194/gmd-6-429-2013, 2013.

Yair, Y., Lynn, B., Price, C., Kotroni, V., Lagouvardos, K., Morin, E., Mugnai, A., and Llasat, M. d. C.: Predicting the potential for lightning
activity in Mediterranean storms based on the Weather Research and Forecasting (WRF) model dynamic and microphysical fields, Journal
of Geophysical Research: Atmospheres, 115, https://doi.org/10.1029/2008JD010868, 2010.